HIGHLY EFFICIENT SPECTRAL CALIBRATION METHODS FOR SWEPT-SOURCE OPTICAL COHERENCE TOMOGRAPHY

A Thesis

by

OSCAR JOSEU PACHECO BARAJAS

Submitted to the Office of Graduate and Professional Studies of
Texas A&M University
in partial fulfillment of the requirements for the degree of

MASTER OF SCIENCE

Chair of Committee,	Sebastian Hoyos
Committee Members,	Javier A. Jo
	Kamran Entesari
	Raffaella Righetti
Head of Department,	Miroslav M. Begovic

August 2017

Major Subject: Electrical Engineering

ABSTRACT

Recent techniques in optical coherence tomography (OCT) make use of specialized light sources that sweep across a broad optical bandwidth, allowing for longer depth ranges at higher resolutions.The produced light source signal can be described as a gaussian damped sinusoid that non-uniformly sweeps across a narrow frequency band. When sampling this interferometric signal uniformly, the generated images present considerable distortion, because the spectral information is a function of wavenumber "k", not time. To solve this problem a "calibration" step needs to be performed; in this process, the acquired interferogram signal is linearized into k-space. The process usually involves estimating the phase-frequency change profile of the SS-OCT system via Hilbert transformation, inverse tangent and phase unwrapping.

In this thesis, a multitude of low complexity, computationally efficient methods for the real-time calibration of Swept Source Optical Coherence Tomography (SS-OCT) systems are implemented and results are evaluated against commonly performed calibration techniques such as Hilbert transformation. Simulation shows execution times decisively improved by up to a factor of ten, depending on the used technique. Axial resolution was also slightly improved across all the tested techniques. Moreover, the inverse tangent and phase unwrapping steps necessary for Hilbert transform calibration techniques are eliminated, vastly reducing circuit implementation complexity and making the system suitable for future inexpensive, power efficient, on-chip solutions in SS-OCT post-processing.

DEDICATION

To my mother, for it is her love, encouragement, and constant support that has guided me along the way.

ACKNOWLEDGMENTS

I would like to thank all those who contributed in some manner to the work described in this thesis. First and foremost I would like to thank my graduate advisor, professor Sebastian Hoyos, for his constant support and for providing me with intellectual freedom. It was through his guidance that this thesis came to be at all, his appreciation for innovative ideas and his support for my attendance to multiple conferences contributed undoubtedly to generate the core ideas for this work. I'd also like to thank my lab mate, Mr. Amir Tofighi, for his friendship and meaningful conversations and for his help obtaining the results and implementing the algorithms shown in this work. lastly, I would like to acknowledge the Mexican council of science and technology (CONACYT) for financially supporting my graduate studies.

CONTRIBUTORS AND FUNDING SOURCES

Contributors

This work was supported by a thesis committee consisting of Professor Sebastian Hoyos [advisor], Professor Raffaella Righetti, and Professor Kamran Entesari of the Department of Electrical Engineering, and by Professor Javier Jo of the Department of Biomedical engineering.

The data analyzed for this work was provided by Mr. Michael Serafino of the department of Biomedical Engineering.

All other work conducted for the thesis (or) dissertation was completed by the student independently.

Funding Sources

Graduate study was supported by a scholarship from the Mexican council of science and technology (CONACYT).

NOMENCLATURE

OCT	Optical Coherence Tomography
OLCR	Optical Low Coherence Reflectometry
OFDI	Optical Frequency-domain Imaging
MZI	Mach-Zehnder Interferometer
SS-OCT	Swept-Source Optical Coherence Tomography
TD-OCT	Time-Domain Optical Coherence Tomography
FD-OCT	Fourier Domain Optical Coherence Tomography
SD-OCT	Spectral-Domain Optical Coherence Tomography
FPGA	Field-Programmable Gate Array
CPU	Central Processing Unit
ADC	Analog to Digital Converter
DAC	Digital to Analog Converter
VCSEL	Swept vertical cavity surface-emitting lasers
FDML	Fourier domain mode locked laser
SLED	Superluminescence diode
TSLED	Tunable SLED
SNR	Signal to noise ratio
SOA	Semiconductor Optical Amplifier
MEMS	Micro-electro-mechanical systems
RIN	Relative Intensity Noise
FWHM	Full-Width Half Maximum

PSF	Point-spread Function
DFT	Discrete Fourier Transform
IpDFT	Interpolated discrete fourier transform
FFT	Fast Fourier Transform
FFP-TF	Fiber Fabry-Perot tunable filters
VT-DBR	Vernier-tuned distributed Bragg reflector
DT-SS	Dispersion Tuning Swept Sources
ASE	Amplified spontaneous emission

TABLE OF CONTENTS

Page

LIST OF FIGURES

FIGURE Page

LIST OF TABLES

1. INTRODUCTION AND THEORETICAL BACKGROUND

This section does not aim to provide the reader with a comprehensive introduction to the vast fields of Optical coherence tomography (OCT) and Optical frequency-domain imaging (OFDI), but rather with a succinct summary of what I consider to be the most critical concepts necessary to understand the present work. However, one could easily utilize the works referenced in this thesis as a starting point, if a full literary review is of interest.

In the following sub-sections, the fundamental operating principles of the discussed imaging technique and others are discussed, together with some information on the different optical light source technology employed. This is done in an effort to elucidate the motivation behind all the employed calibration techniques and their potential applicability to both commercial and research/academic environments.

1.1 Motivation

Current SS-OCT systems perform most of the signal processing required to obtain high resolution brightness maps and 3D images "offline"; meaning they make use of external processing units such as personal computers running third party software, however, the use of full personal computers and licensed software can both add to the overall cost of the system, and ameliorate its efficiency. This creates an opportunity for signal processing, embedded and mixed-signal oriented people to develop, test and implement on-chip solutions that would perform the necessary operations on a printed circuit board, improving cost, complexity and eventually leading to the development of portable, point-of-care devices that can positively affect the adoption of the technology, ultimately improving the accurate diagnosis of a number of pathologies.

1.2 Optical Coherence Tomography

Optical Coherence Tomography (OCT) is a noninvasive imaging technique capable of generating cross-sectional images of tissue architectural morphology with high axial resolution [1]. Since its introduction as a non-invasive crosssectional imaging technique with a spatial resolution of a few micrometers back in 1991 [2], Optical Coherence Tomography (OCT) has been actively developed and commercialized to the point of becoming a highly efficient medical imaging tool for the accurate diagnosis of a wide variety of pathologies, especially those of interest in the area of cardiology, optometry, and ophthalmology. Recently, Optical Coherence Tomography has established itself as the de-facto biomedical imaging modality when low penetration and high resolution are desired. The technology has made its way into a wide array of applications and fields ranging from biomedical imaging to archeology. This rapid adoption growth can be attributed at least in part to the techniques ability to capture high-resolution cross-sectional images without touching the eye [18]. In the most basic OCT apparatus, back scattered photons from a tissue of interest are detected using a Michelson interferometer; depth information is then extracted, from which an image is reconstructed. Subsequently, more advanced techniques that exploit this basic principle of operation have emerged. Early embodiments of the technique existed as a time domain interferometric technique in which each depth-dependant reflection, corresponds to a different time delay. Each delay is then measured by manually moving the reference arm of the Michelson interferometer so that depth information can be obtained at distinct times, making the information time encoded; hence the time domain OCT or TD-OCT name.[19] Later, the need for faster acquisition speeds has pushed towards more elegant techniques in which the reflection coefficient information is obtained via the Fourier transform in the wavenumber space (k-space), these techniques are generally refered to as Fourier domain OCT (FD-OCT).

1.2.1 Operating Principles

Optical coherence tomography is fundamentally based on the one dimensional technique called "optical low coherence reflectometry" (OLCR) [33] which employs a Michelson interferometer to detect back reflected light from a sample arm. A Michaelson interferometer works by splitting from a low coherence source into two directions, usually referred to as the reference arm and the sample arm. In an optical fiber based implementation of a Michaelson interferometer, light in the reference arm is directed back after reflection from a mirror to a 2x2 fiber coupler, where it gets combined with the backscattered light from the sample in the sample arm in order to generate an interference pattern that contains information about the depth reflectivity profile of the sample.

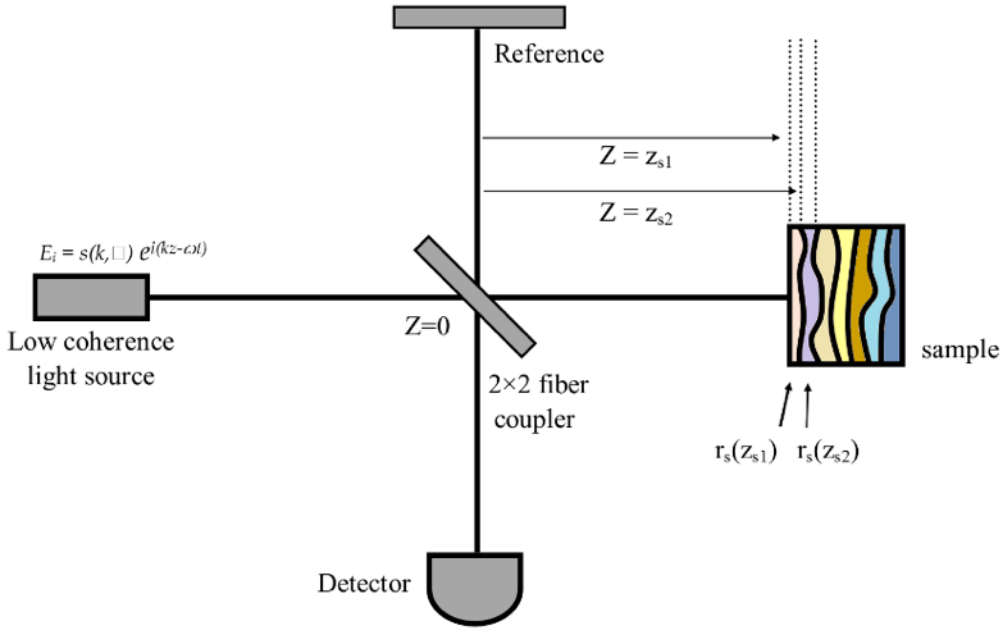

Figure 1.1: Michelson interferometer-based OCT system. A reference mirror and a beamsplitter are used to produce an interference signal at the detector.

To understand the basics of image formation in an OCT system, consider the simplest case in which the sample is modeled as a collection of N discrete reflectors having electric field reflectivities $r_{s1}, r_{s2}, \cdots, r_{sN}$ and located at the distances $z_{s1}, z_{s2}, \cdots, z_{sN}$ from the beamsplitter as shown in Figure 1.1. The depth-dependant reflectivity profile is then $r_s(z_s)$, such a sample can then be mathematically represented as a sum of Dirac-delta pulses by: $r_s(z_s) = \sum_{n=1}^{N} r_{sn}\delta(z_s - z_{sn})$ by definition the power reflectivity is equal to the magnitude squared of its electric ïňĄeld reflectivity, that is given by $R_{sn} = |R_{sn}|^2$. Diferentiation is then obtained by reconstructing $r_s(z_s)$ from the measurements. The light source electric field can be expressed as $E_i = s(k,\omega)e^{i(kz-\omega t)}$, where $s(k,\omega)$ represents monochromatic light contribution to the electric field amplitude of the polychromatic light with a wavenumber $k = (2\pi/\lambda)$ and an angular frequency $\omega = 2\pi\nu$. As usual, the wavelength λ and frequency ν are related by the refractive index $n(\lambda)$ of the medium of propagation as$n(\lambda) = c/\nu\lambda$, where c denotes the velocity of light in vacuum. The electric field of the light passing through the 50/50 beam-splitter after getting reflected from the sample can then be expressed as $E_s = E_i/\sqrt{2}(r_s * e^{i2kzs})$, where * denotes convolution, the $1/\sqrt{2}$ represents 50% reduction in light intensity due to the beam-splitter, lastly, the factor of 2 in the exponential term represent the round-trip path of the light in the sample arm. The expression for E_s can be simplified to $E_s = E_i/(\sqrt{2}(r_s * e^{i2kzs_n})$, Similarly the expression for the reference arm electric field can be expressed as $E_R = E_i/(\sqrt{2}(r_R * e^{i2kz_R})$ The interference signal detected at the photo-detector$ID(K)$ is the time average of the intensity signal resulting from the phasor sum of E_R and E_S expressed by:

$$I_D(k,\omega) = (\rho/2)\langle|E_R + E_S|\rangle \tag{1.1}$$

where ρ denotes the responsivity of the photodetector and the factor of 2 reflects the halving of intensity on the second pass of light through the beam-splitter. Simplifying the

above expression based on the fact that the electric field oscillations are much faster than the responsivity of the photodetector, we get an expression involving only time invariant terms as:

$$I_D(k) = \frac{\rho}{4}[S(k)(R_R + R_{S1} + \cdots + R_{SN})]+ \tag{1.2}$$

1.2.2 OCT Techniques

Over the past two decades, multiple techniques involving OCT have been introduced. These can be categorized into three main generations based on performance, reliability, and implementation. First generation techniques relied on the physical movement of the fiber or optical path for tissue penetration and image reconstruction. This mechanical time-varying movement led to it's reference as time domain OCT (TD-OCT), which uses a single-element photodetector to acquire the fringe signal serially. This technique suffers from limitations such as a slow scan speed and lower axial resolution; the second and third generations of OCT techniques can be further categorized as Fourier Domain OCT (FD-OCT).

In FD-OCT techniques, the spectral information of the interferogram is measured and the reflection coefficient information is obtained via the Fourier transform in the wavenumber space (k-space) to generate a depth dependant brightness map, commonly known in tomography as B-scan. These techniques are very similar in concept as no mechanical movement of the interferometer arm is involved, but they differ in execution. The first of these techniques is referred to as spectral domain OCT or SD-OCT for short; in this technique information is obtained by sequentially measuring different wavelengths generated from a broadband optical source using a spectrometer and a multi-channel analyzer. While the axial resolution is improved from TD-OCT techniques, the acquisition speed is limited by the spectrometer and analyzer, also the use of high speed cameras as detec-

tion devices can be quite costly, especially in the 1060nm to 1310nm wavelengths [12]. The third generation OCT technique is known as swept source optical coherence tomography (SS-OCT). In these technique spectral discrimination is achieved by rapidly tuning a narrowband light source over a broad optical bandwidth. Since all the light is collapsed into a single wavelength that is consequently swept across a wide range, better signal to noise ratios, faster speeds, a better sensitivity roll-off, and tissue penetration compared to SD-OCT is achieved [13].

Swept Source Optical Coherence Tomography (SS-OCT) systems employ a short-cavity laser source that sweeps across a narrow band of wavelengths with each scan, these lasers have a wavelength typically centered at approximately 1 Âŧm and can achieve very high imaging speeds up to 150,000 per second [34] allowing for fast and accurate diagnosis; this is particularly important in areas such as angiography where the patient is asked to hold still for three to four seconds in order to retrieve a 3mm by 3mm image, larger images would prove nearly imposible as it is very difficult for a patients eye movement to remain still for longer periods of time. Moreover SS-OCT exhibits higher axial resolution and an improved signal-to-noise ratio compared to SD-OCT [2], additionally, swept light sources are invisible, making them more suitable for a diagnostics environment as they are less distractive. Finally, the longer wavelength exhibited by swept sources provides a better sensitivity roll-off over the entire scan window, which delivers the ability to obtain clear images of deeper tissue.

In the following subsections a brief review of the main Optical Coherence Tomography techniques is presented, starting with time-encoded OCT and following with the two most common FD-OCT techniques.

1.2.3 TD-OCT

In this iteration of the technology, the reference arm of a Michelson's interferometer is mechanically moved along an axis, causing the information to be time-encoded, hence the Time-Domain name for the technique. This mechanical movement causes it to suffer from lower ranging accuracy and slow tinning speed when compared to modern Fourier transform based techniques that utilize a less complex setup and no mechanical movement of the reference arm, and can potentially achieve much higher axial resolutions. The following figure represents a common TD-OCT setup.

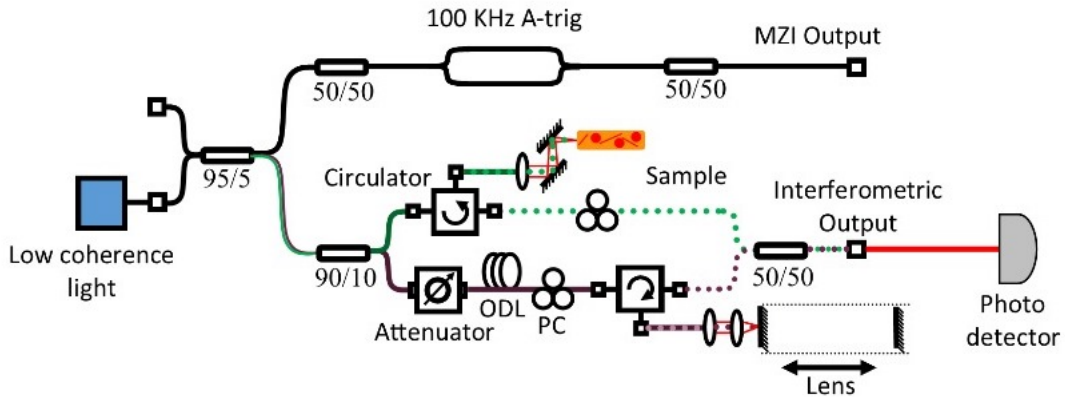

Figure 1.2: Time Domain, Michelson interferometer-based OCT system. A reference mirror is mechanically moved across an axis to resolve the depth dependant coefficients.

1.2.4 FD-OCT or Optical Frequency-domain Imaging

Fourier transform based techniques (Also refered to as Optical Frequency-Domain Imaging) utilize a less complex setup that requires no mechanical movement of the interferometer reference arm, which provides robustness, much higher acquisition speeds compared to time-encoded techniques and can potentially achieve much higher coherence

lengths and hence axial resolutions. These techniques are also refered to as Fourier domain OCT (FD-OCT). In such techniques, either a broadband optical source or a narrow band, swept-tuned laser is used as a light source, spectral information of the interferogram is measured and the reflection coefficient information is obtained via the Fourier transform in wavenumber space. Fourier domain OCT can be mainly implemented in two ways: spectral domain OCT (SDOCT), using a broadband light source and a spectrometer with a multi-channel analyzer and an expensive InGaAs camera, and swept source OCT (SSOCT), using a broadband narrow-pulse swept-laser source and a single InGaAs photodetector.[19]

Each of these techniques have their advantages and drawbacks, however, due to the recent advancements in swept source technology and the generally higher cost associated with spectral analyzers and broadband optical cameras, swept source OCT related research and implementations have thrived in the last years over SD-OCT techniques.

1.2.5 SD-OCT

In this technique, a broadband light source and an in-line optical camera are used in an interferometric setup to consequently acheive spectral discrimination by means of Fourier transformation, eliminating the need for mechanical movement of the reference arm, this technique exhibits decisively faster scanning speeds and axial resolutions compared to TD-OCT techniques, however, they exhibit a high cost due to the broadband optical sources and detectors and a relatively more complex set up than other FD-OCT techniques (namely SS-OCT and its variants).

1.2.6 SS-OCT

The third generation OCT technique is known as swept source optical coherence tomography (SS-OCT). In these technique spectral discrimination is achieved by rapidly tuning a narrowband light source over a broad optical band-width. Since all the light is

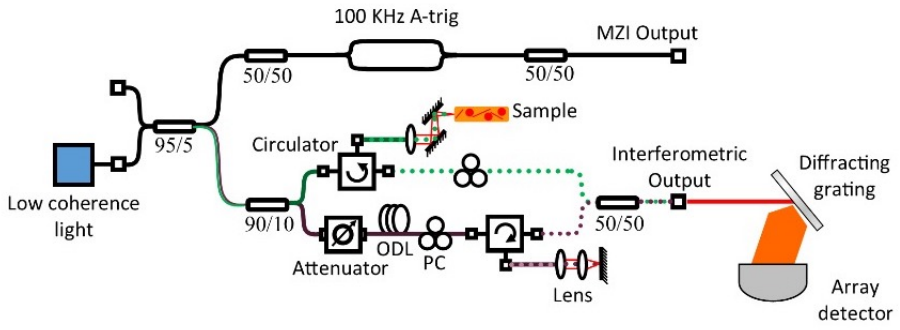

Figure 1.3: Spectral-domain based OCT system. A reference mirror remains fixed, as a broadband light source is used to resolve the depth dependant coefficients.

collapsed into a single wavelength that is consequently swept across a wide range, better signal to noise ratios, faster speeds, a better sensitivity roll-off,and tissue penetration compared to SD-OCT is achieved [13].

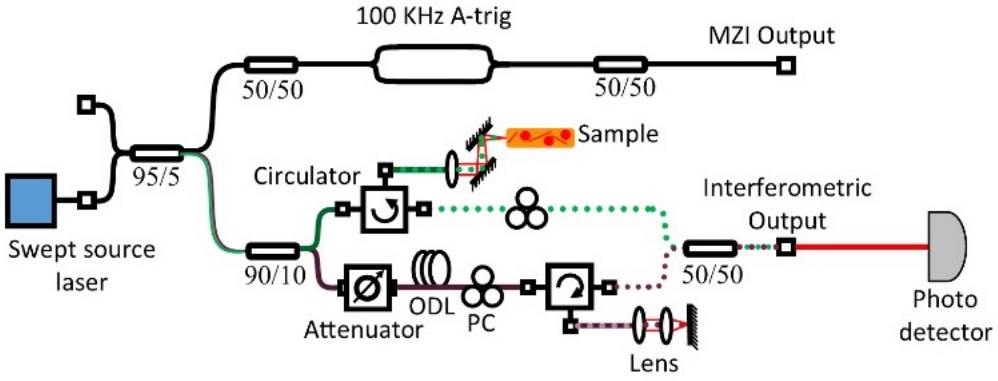

Figure 1.4: Swept-source OCT system. A reference mirror remains fixed, as a "swept" optical source is used to resolve the depth dependant coefficients.

1.2.7 The Need For Multi-MHZ SS-OCT

Recently, there's a growing interest in producing volumetric representations of tissue using OCT [35], since both SD-OCT and SS-OCT setups output single lines (A-lines) that need to be stacked together to create B-Scans, such systems are only able to produce a 3-D volumetric map (C-scan) via post-processing. First, a series of B-scan OCT images is acquired from distinct transverse locations in the sample, the resulting sections are then "stacked" to generate a volumetric representation of the sample's cross section. Consequently, in SS-OCT, the time required to create such 3D Volume is determined by the time required to collect all 2D sections plus the time taken by the software to stack them together. To this end, recent progress in SS-OCT has lead to multi-MHz A-scan line rates [34]. A 5 MHz line rate for instance allows a B-scan image of 500 lines to be created in 0.1 ms. If 500 such frames of 500 pixels in depth in the A-scan are acquired, this means a volume of 5003 of pixel data captured in approximately 0.05 s [34]. Aside from the necessary high speed to keep acquisition time short, and the extra processing step, the acquisition of volumetric data needs a considerable amount of storage space (0.8Gs/s per channel or 1.5 Gbytes per volume) to be acquired successfully. In this work, efficient algorithms and proposed low complexity hardware implementations are presented as a solution for high speed processing of volumetric OCT images in real time.

2. THE "CALIBRATION" PROBLEM

In typical swept-source OCT (SSOCT), spectral information is acquired sequentially using a single InGaAs photodetector while rapidly sweeping the wavenumber of a narrow-band light source over a broad optical bandwidth. However, due to some particularities of the employed optical swept sources (refer to section 1.3) this sweeping profile might not be perfectly linear depending on the kind of source employed. This has lead to the use of an auxiliary device to create a reference clock used to re-sample the signal at the correct time indexes. Usually a Mach-Zehnder interferometer (MZI) is employed as a reference path to either create a non uniform clock that follows the phase profile of the laser by hardware means (conventionally using the zero crossings of the signal) or to calibrate the sample interferometer signal in post processing. This MZI reference signal can be described as a Gaussian damped sinusoid that non-uniformly sweeps across a narrow frequency band, this non-uniform sweep, follows the sweeping profile of the interferometer's sample path. When sampling the interferometric signal uniformly without the use of some re-sampling technique, the generated images present considerable distortion, as the spectral information is a function of wavenumber "k", not time. In order to solve this problem, calibration needs to be performed; in this process, the acquired interferogram signal is linearized into k-space. The process usually involves estimating the phase-frequency change profile of the SS-OCT system via Hilbert transformation, inverse tangent and phase unwrapping. [20] The following figure shows a representation of a typical MZI signal and it's instantaneous phase profile, corresponding to the non linear sweep associated the optical source, this profile is sometimes referred to as the "calibration profile" as it is used to interpolate the interferometric signal at corrected k-linear instances.

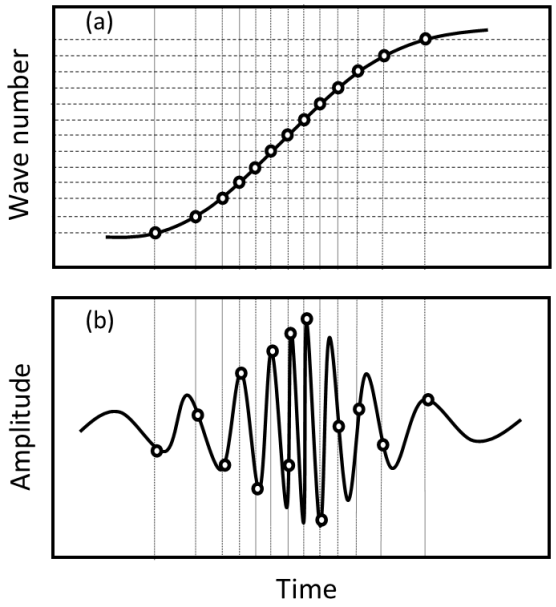

Figure 2.1: Instantaneous phase linearization (a): unwrapped phase of the MZI (b): MZI signal representation. Dots depict sampling indexes.

2.1 Common Calibration Techniques

Approaches to calibrate the non-uniform sweep can be further organized into two main categories. Those that are done in post-processing (offline) and those performed in real-time (online).

2.1.1 Spectral Phase-based Techniques

In these techniques, a curve describing the change in instantaneous frequency of the MZI is obtained in post processing by unwrapping the instantaneous phase of a simple Mach-Zehnder interferometer [5] (Fig. 2.1).

Knowing the physics of how an MZI signal is created, its amplitude can be expressed as:

$$I_{MZI}(t) = Cs(t)\cos\left(\Delta\phi(t)\right) \tag{2.1}$$

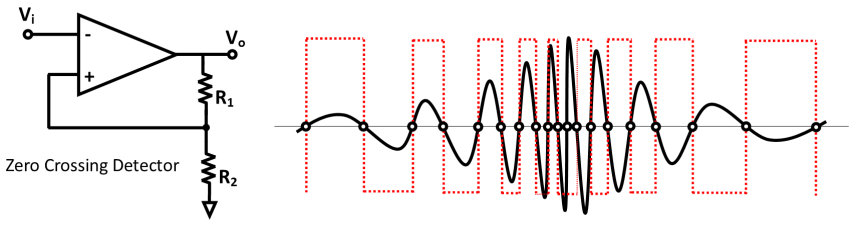

Figure 2.2: Simple zero crossing detector (left) ($R_1 \gg R_2$). Clock signal generated at zero-crossings (right).

Where C is a constant, s(t) is the spectral shape of the emitted laser beam and $\Delta\phi$ is the phase difference between the two photons added up on the reciever coupler in an MZI. Conventionally Hilbert transformation is used to extract the instantaneous phase of the MZI signal $\Delta\phi$ [4]. Figure 2.1 shows a common calibration trace demonstrating the instantaneous phase $\Delta\phi$ of an MZI signal, an example of a k-linear sampling time stamps is also shown.

2.1.2 Generic Real-time Calibration techniques

In the most widely accepted online calibration technique, the zero-crossings in a Mach-Zehnder interferometer (MZI) are used to generate a non-uniform clock [6]. As these points are determined in time sequence, they are used to index the data set of the simultaneously captured spectral interferogram. Thus, the OCT signal is transformed into a set of data with identical intervals of wavenumber (k) before the Fast Fourier Transform (FFT), this scheme is shown in Fig. 2.2. In general, software-based methods are the more popular alternative for re-sampling and typically employ interpolation to calibrate the signal in linear k-space intervals. Usually, longer computational times are associated with these generally more complex interpolating functions, but typically lead to better images.

3. CALIBRATION BASED ON A SQUARE-LAW ENVELOPE DETECTOR*

Our first proposed low complexity calibration technique, aims to provide an easy to implement re-sampling scheme that would generate a clock whenever the MZI signal passes two, predefined thresholds using a continuous time ternary encoding (CTTE) technique [cttepaper], by implementing this non-uniform sampling clock we aim to construct a device that would linearize the interferometer in k-space while providing the system operator with the flexibility of choosing the desired number of points per A-line, something impossible to do without interpolation in common zero-crossing based re-sampling schemes, an added advantage of the proposed method is that only one acquisition channel is needed, effectively cutting the required storage by half. For the CTTE block to work without the need for dynamically changing threshold levels, a constant amplitude signal is needed. In order to remove the amplitude information of the MZI signal we implemented a very well known demodulation scheme known as a square-law detection, which extracts the envelope of an amplitude modulated signal by means of squaring and low pass filtering and then divides the original signal by its detected envelope. This produced a signal with a constant amplitude term.

3.1 Amplitude Correction by Means of Square-law Envelope Detection

Envelope detection is the process by which the baseband message in an amplitude modulated signal is retrieved. For our proposed method a square law envelope detector was used, which exhibits significantly lower complexity. We show here that the square-law envelope detection provides results at a par with the Hilbert transformation based demodulators for the purpose of k-domain calibration.

*2016 IEEE. Reprinted, with permission, from A. T. Zavareh, O. Barajas, M. Serafino, J. Jo, B. Applegate, B. M. Sadler, and S. Hoyos, "A novel continuous time ternary encoding based SS-OCT calibration," 2016 IEEE Biomedical Circuits and Systems Conference (BioCAS), 2016.

An amplitude modulated signal can be described by Eq.3.2, where $m(t)$ is the baseband message, $A_c \cos(\omega_c t)$ is the carrier wave, k_a is the amplitude sensitivity of the modulator and $1 + k_a m(t)$ is the envelope of the signal. The baseband message $m(t)$ is a low pass signal with cut-off frequency Ω, that is $M(\omega) = 0$ for $|\omega| > \Omega$.

$$I_{MZI}(t) = A_c[1 + k_a m(t)] \cos(\omega_c t) \tag{3.1}$$

The squarer output is then:

$$I^2_{MZI}(t) = \frac{1}{2} A_c^2 [1 + k_a m(t)]^2 + \frac{1}{2} A_c^2 [1 + k_a m(t)]^2 \cos(2\omega_c t) \tag{3.2}$$

The first term on the right-hand side is a low-pass signal except that the cutoff frequency has been increased to 2Ω by the squaring operation. The second term has a spectrum centered at $2\omega_c$.

The squared signal now needs to pass through a filter $H(\omega)$ which is a low pass filter with cutoff frequency 2Ω, whose ideal output is then:

$$y(t) = \frac{1}{2} A_c^2 [1 + k_a m(t)]^2 \tag{3.3}$$

Finally, taking the square root gives an output proportional to $m(t)$ with a DC offset. No decimation step is needed as we wish to trace the full cycle of the wave. Once the envelope information has been extracted, in order to bring the amplitude of the MZI signal to a constant level, it is necessary to divide the original MZI signal by the output of the undecimated envelope detector. Our envelope detector was implemented digitally, and simulation showed that a very low complexity 4 tap, linear phase, half band FIR filter is sufficient for this digital demodulator to accurately estimate the signal's envelope as shown in Fig. 3.1, without compromising the axial resolution of the ultimately calibrated images.

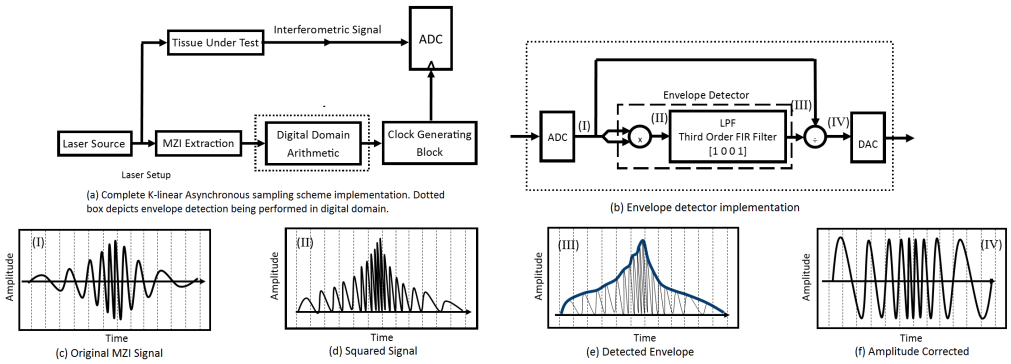

Figure 3.1: Envelope detection process from a continuous time perspective. Figures (c) to (f) correspond to points I-IV in (b), respectively.

After the amplitude correction step, a continuous time ternary encoding scheme was implemented to generate a k-dependent clock as illustrated in Fig. 3.2. This circuit generates a pulse whenever the amplitude of the MZI signal exceeds a predefined ternary encoded level-sampling threshold.

3.2 Continuous Time Ternary Encoding (CTTE)

The proposed linearization method employs an encoding technique known as Continuous Time Ternary Encoding (CT-TE) [5] to generate a k-domain sampling clock for the interferometer signal. The CT-TE only fires when an amplitude variation crosses some predefined thresholds. In our implementation a threshold set ($V_{th,L}, V_{th,H}$) was defined forming an input tracking window and subsequently stored in a lookup table. Depending on the comparison results, the sum module generates ternary state ”1” or "-1" as $x(t)$(CTTE input) goes higher than $V_{th,H}$ or lower than $V_{th,L}$, respectively; otherwise, it holds an output of "0" unchanged.

3.2.1 CTTE Threshold Determination

By defining a parameter N, that divides the unit circle (Figure 3.2) in equidistant rotational intervals, our CT-TE provides the advantage of defining the number of output

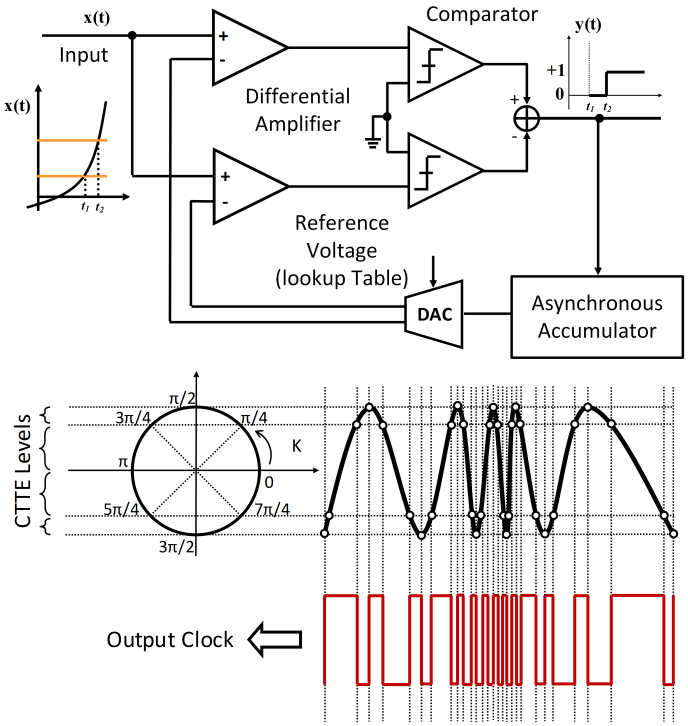

Figure 3.2: Continuous time level crossing circuit implementation (top): continuous time ternary encoding (CTTE) (bottom): K-linear clock generation example, with N=8 CTTE levels

values per signal cycle, giving the system designer flexibility to choose a determined output points. This in turn eliminates the need for changing the MZI length path, as enough points can be retrieved by choice of the threshold values. The non-uniform k-domain characteristics of the simultaneously acquired interferometer signal $\Delta\phi$ are effectively linearized by asynchronously sampling using this non-uniform, real time clock, generated by the proposed thereshold level technique.

3.3 Results

In order to evaluate the performance of our proposed calibration scheme simulation was performed using SIMULINK. Performance of the proposed method in terms of image quality was investigated by computing the axial resolution obtained over 500 realizations

and three different arm depths, while modifying key variables such as MZI signal ADC resolution and N parameter choice. Fig.3.3 shows the mean axial resolution for 500 a-lines in terms of input ADC resolution and choice of N. Axial resolution remains constant throughout all tested ADC resolutions implying that our proposed scheme can be used to significantly relax ADC specifications without resolution loss, which translates to an immediate power saving advantage. As stated in [9] every single ADC bit reduction can cut the power consumption by a factor of at least four. As Fig.3.3 implies the axial resolution was constant sweeping the ADC bit from 14 to 8. That means a factor of approximately 4096 can be saved in terms of the MZI sampling ADC power consumption.

Axial resolution remains fairly constant regardless of the choice of N. However, it is important to note that by setting N to a convenient number, the system designer can specify the number of points per cycle desired for efficient FFT calculation and b-scan reconstruction, which constitutes an advantage for real time implementation as this is typically performed by elongating or contracting the optical path of the Mach-Zender interferometer(MZI) as described in Eq.3.5 [8],

$$I_{MZI}(t) = Cs(t)\cos\left(2\pi k(l_2 - l_1)\right) \tag{3.4}$$

where l_1 and l_2 are the interferometer arm lengths.

Finally we measured the sensitivity roll-off across seven sample arm depth indexes, as shown in Fig.3.3. it is evident that choice of N has a negligible effect on roll-off. For our particular setup a value of N=8 yielded the best results from those tested.

Our proposed resampling scheme shows a much lower complexity than the spectral phase interpolation methods, that typically use a filter consisting of tens of coefficients to realize Hilbert transformation. Recently an 18 coefficient FIR filter Hilbert transform implementation was demonstrated [10]. The authors found the main filter block by sys-

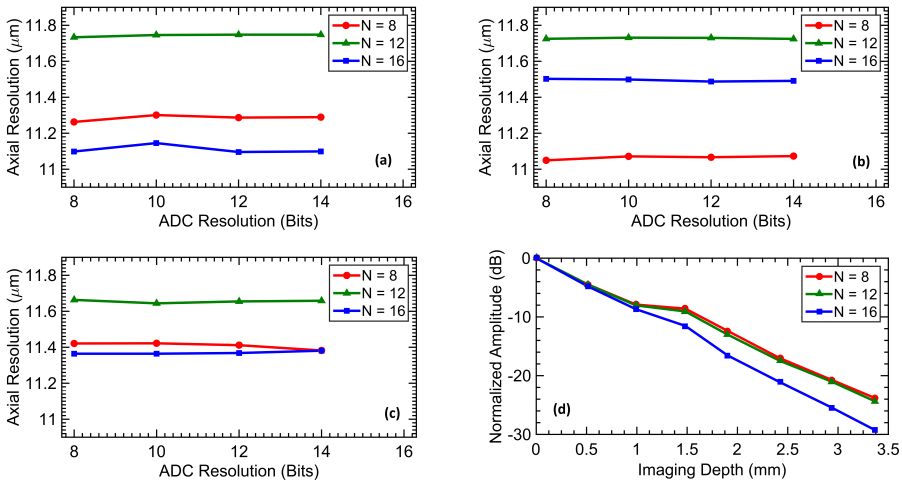

Figure 3.3: Axial resolution mean value (a) to (c) different sampling arm lengths (a:514μm-b:998μm-c:1483μm), across 500 realizations as a function of ADC resolution (8bits-14bits) and N (d): sensitivity roll-off across all depths.

tematically changing the filter order while observing axial resolution, such that 18 coefficients are needed so that no artifacts such as ghosting are produced. Their axial resolution plateaued at 8 coefficients, showing significant artifacts and image ghosting. On the other hand, the main filtering block on our scheme is based on a much simpler 4 tap FIR filter.

As Table 3.1 suggests, our axial resolution results are tantamount to those obtained by performing traditional spectral phase calibration methods. Those shown in the bottom table are obtained from a theoretical Hilbert transform and not from an FIR implemented one. In terms of image quality our results are on a par with those obtained by offline interpolation methods. It can be clearly observed in Fig.3.4 that for image reconstruction, the choice of N has little effect on the overall quality of the image.

As discussed above, a significant reduction in the MZI ADC bit is achieved, the core arithmetic is massively reduced whilst the resolution remains constant.

Table 3.1: Comparison between the axial resolution of the proposed method and the theoretical spectral phase-based technique. Proposed Method (Top). Spectral phase-based (Bottom). All quantities are in μm

N	*Depth (μm)*		
	514	998	1481
8 [$Cycle^{-1}$]	11.28	11.07	11.38
12 [$Cycle^{-1}$]	11.74	11.72	11.68
16 [$Cycle^{-1}$]	11.09	11.49	11.38
Quasi N	*Depth (μm)*		
	514	998	1481
8 [$Cycle^{-1}$]	11.10	11.10	11.09
12 [$Cycle^{-1}$]	11.11	11.11	11.14
16 [$Cycle^{-1}$]	11.13	11.12	11.12

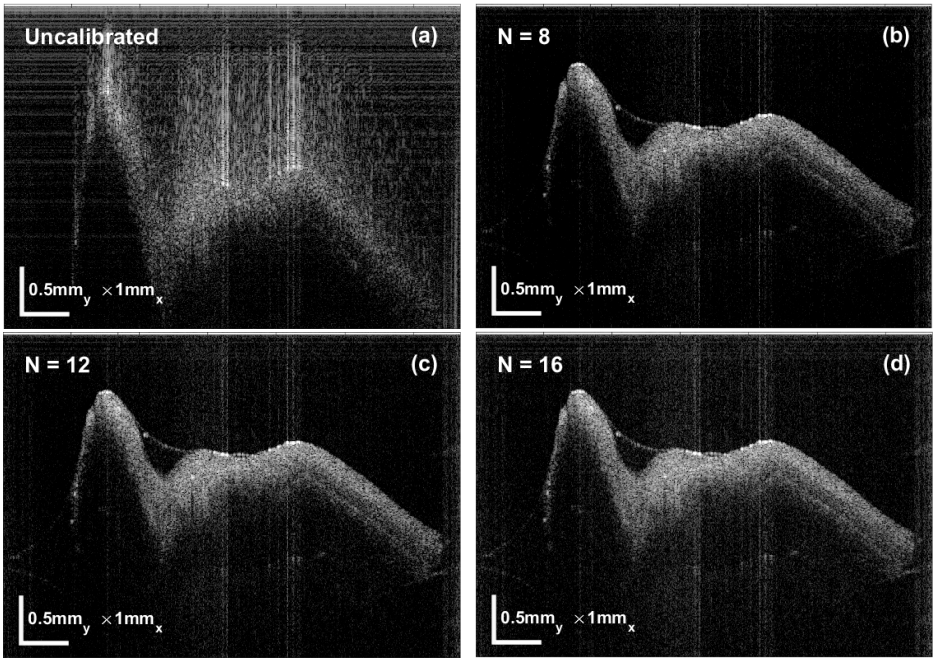

Figure 3.4: Image reconstruction comparison. (a) Uncalibrated. (b) through (d), increasing number of angular quantization levels N.

3.4 Conclusion

In this section, we have leveraged a novel, computationally efficient, less power consuming approach for spectral calibration of swept sources using a square law envelope detector and a continuous time ternary encoder (CT-TE) sampler. A corrected k-linearized clock was extracted from a simple Mach-Zehnder interferometer (MZI) and then used to re-sample the interferometer signal at the corrected time indexes. Axial resolution showed results on par with a conventional spectral phase-based calibration technique while maintaining a significantly reduced computational complexity enabling for online implementation of the method.

4. KALMAN FILTERING BASED CALIBRATION*

Although faster algorithms for simple calibration have been presented [14], none of these algorithms account for the presence of noise in the input signal. This can limit their application in ultra low cost, custom OCT systems. The main motivation for this work is to provide a framework that facilitates less complex implementation of cost effective swept sources and ultimately lead to a wider adoption of the technology.

4.1 Setup

A custom-built SS-OCT system (Fig. 4.1) was used for acquisition; it is comprised of a broadband Swept source (ESS, Exalos) with a center wavelength of 1310 nm and 150-kHz sweep rate. The signals were aquired using a 14-Bit 250 MS/s digitizer Module (NI5761, National Instruments).

As shown in Fig. 4.2, the digitally acquired MZI signal data is fed into an Extended Kalman Filter algorithm block that estimates the instantaneous phase, which is then processed by the comparison step block (Fig. 4.4) to create an asynchronous K-linear clock. This CLK signal is then used to acquire the interferometric signal at the correct time instants.

4.1.1 Estimation

For the estimation of the MZI signal instantaneous frequency ϕ an Extended Kalman Filter (EKF) was used (Fig. 4.2). An Extended Kalman Filter is generally used to estimate the values of inner state variables of a non-linear system model with known outputs and noise statistics [15]. This poses multiple implementation challenges due to some pecu-

*2017 IEEE. Reprinted, with permission, from A. T. Zavareh, O. Barajas and S. Hoyos, "An Efficient Estimitaion Algorithm for the Calibration of Low-Cost SS-OCT Systems," 2017 IEEE 14th International Symposium on Biomedical Imaging (ISBI), Melbourne, Australia, 2017.

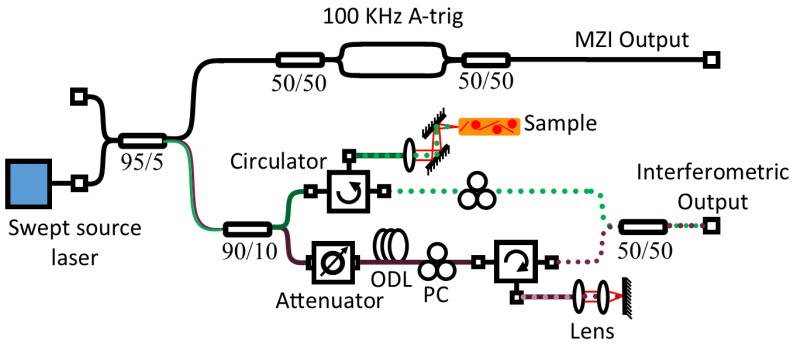

Figure 4.1: SS-OCT optic elements configuration. PC: polarization controller, ODL: optic delay line.

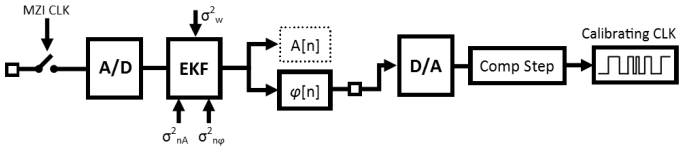

Figure 4.2: Estimation technique block diagram. σ_w^2 is the measurement noise power. $\sigma_{n_A}^2$ is the amplitude noise power. $\sigma_{n_\phi}^2$ is the instantaneous phase noise power

liarities of the MZI signal such as the chirp not being constant in amplitude, the instantaneous phase not increasing monotonically, and the phase being highly noisy. However, all of these were overcome by generating an accurate state space model as subsequently described.

State Space modeling: A nonlinear state space model can be written as:

$$\begin{aligned} \mathbf{X}[n] &= f(\mathbf{X}[n-1], \mathbf{N}[n-1]), \\ \mathbf{Y}[n] &= h(\mathbf{X}[n], \mathbf{W}[n]), \end{aligned} \tag{4.1}$$

where $\mathbf{X}$ is the matrix of state variables, $\mathbf{N}$ is the state noise, $\mathbf{Y}$ is the output measurements, and $\mathbf{W}$ is the measurement noise.

4.1.1.1 State equations

The state variables are constructed as follows [15],

$$\mathbf{X}[n] = \begin{bmatrix} A[n] & \phi[n] & \phi^{(1)}[n] & \phi^{(2)}[n] & \phi^{(3)}[n] \end{bmatrix}, \tag{4.2}$$

where ϕ is the instantaneous phase, $\phi^{(n)}[n]$ is the n^{th} order derivative of ϕ, and A is the instantaneous amplitude.

A sampled MZI can be modeled as [15],

$$y[n] = A[n]cos(\phi[n]) + \mathbf{W}[n] = A[n]cos(\sum_{i=l}^{M} b_i n^i) + \mathbf{W}[n], \tag{4.3}$$

where b_i are fixed polynomial coefficients. The assumption is that the instantaneous phase profile is ruled by an M^{th} order polynomial behavior.

Using discrete time Taylor expansion, the state update equation can be written as,

$$\mathbf{X}[n] = \mathbf{F}\mathbf{X}[n-1] + \mathbf{N}[n-1] =$$

$$\begin{bmatrix} 1 & 0 & 0 & 0 & \cdots & 0 \\ 0 & 1 & \frac{1}{1!} & \frac{1}{2!} & \cdots & \frac{1}{M!} \\ 0 & 0 & 1 & \frac{1}{1!} & \cdots & \frac{1}{(M-1)!} \\ \vdots & \vdots & \vdots & \vdots & \ddots & \vdots \\ 0 & 0 & 0 & 0 & 0 & 1 \end{bmatrix} \mathbf{X}[n-1] + \begin{bmatrix} n_A[n-1] \\ n_\phi[n-1] \\ n_{\phi^{(1)}}[n-1] \\ \vdots \\ n_{\phi^{(M)}}[n-1] \end{bmatrix}. \tag{4.4}$$

In the above equation, the amplitude of the MZI signal has been modeled as what is known as a random walk in literature [16]. This model assumes that the amplitude in time n differs from the amplitude in time n-1 by a Gaussian, stationary white amplitude noise $n_A[n]$. It can be observed that the phase profile of a typical MZI exhibits a third order polynomial behavior with its second order derivative resembling a random noise

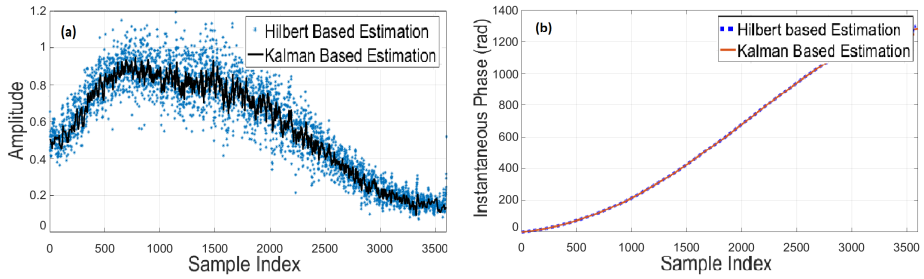

Figure 4.3: MZI signal parameter estimation for a typical realization. (a) Amplitude parameter extraction. (b) Instantaneous phase extraction

due to intrinsic measurement error. This poses a problem as the filter can estimate noise as a constant unless accounted for. Consequently then, any phase profile that exhibits a higher order than two cannot be evaluated. To account for this, we introduce a phase noise parameter $n_\phi[n]$ in Eqn. (4.4) that allows for higher order correlated product determination as shown in Eqn. (4.5).

By accounting for noise in the system, we effectively give the swept source designer the ability to use lower quality photo electric components, significantly reducing the cost of implementation and allowing for a wider adoption of SS-OCT systems.

It can be easily presumed that $n_{\phi^{(l)}}[n] = n_{\phi^{(l-1)}}[n] - n_{\phi^{(l-1)}}[n-1]$. Subsequently, the state noise covariance matrix $\mathbf{V}$, can be written as,

$$\mathbf{V} = Cov(\mathbf{N}) = \begin{bmatrix} \sigma^2_{n_A} & 0 & 0 & 0 & 0 \\ 0 & \sigma^2_{n\phi} & \sigma^2_{n\phi} & \sigma^2_{n\phi} & \sigma^2_{n\phi} \\ 0 & \sigma^2_{n\phi} & 2\sigma^2_{n\phi} & 3\sigma^2_{n\phi} & 4\sigma^2_{n\phi} \\ 0 & \sigma^2_{n\phi} & 3\sigma^2_{n\phi} & 6\sigma^2_{n\phi} & 10\sigma^2_{n\phi} \\ 0 & \sigma^2_{n\phi} & 4\sigma^2_{n\phi} & 10\sigma^2_{n\phi} & 20\sigma^2_{n\phi} \end{bmatrix} \tag{4.5}$$

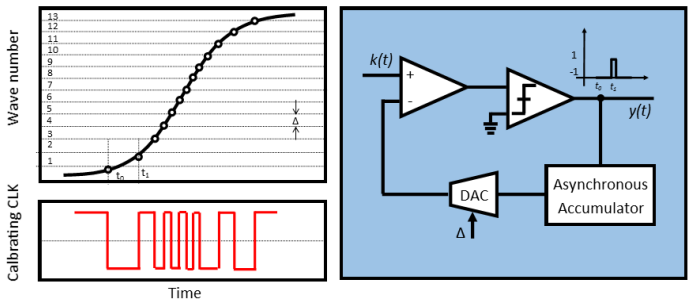

Figure 4.4: Comparison step circuit. (Top left) Equally divided calibration profile. Δ defines the number of points designed to be sampled (wave number quantization interval). (Bottom Left) Calibrating CLK. (Right) Asynchronous time comparison block diagram.

4.1.1.2 Observation equations

Since the parameters this work is trying to estimate are not directly measurable, a nonlinear Extended Kalman Filter model was used to relate state variables to the measured data. Simplifying Eqn.(4.1) we have,

$$\mathbf{Y}[n] = h(\mathbf{X}[n], \mathbf{W}[n]) = x_1[n]cos(x_2[n]) + \mathbf{W}[n], \tag{4.6}$$

where **W**[n] is modeled to be a stationary, white, Gaussian noise with $E\{\mathbf{W}[n]\mathbf{W}[n+k]\} = \frac{\sigma_w^2}{2}\delta[k]$.

This nonlinear equation must be linearized using the Jacobian matrix. That is

$$\mathbf{H}[n] = [h_{ij}]_{1\times(M+2)} = \left.\frac{\partial h_i}{\partial x_j}\right|_{\hat{x}_n^-}, \tag{4.7}$$

where $\hat{x}_n^-$ is a priori state estimate at step n given knowledge of the process prior to step n. That means $\mathbf{H}[n]$ can be written as,

$$\left[cos(\hat{x}_2^-[n]) \quad -\hat{x}_1^-[n]sin(\hat{x}_2^-[n]) \quad 0 \quad 0 \quad 0\right].$$

Once the model is complete and the equations derived, the proposed implementation

for the presented amplitude and instantaneous phase estimation method is shown in Algorithm 1. The addition of amplitude, phase and measurement noise into the state space model improves robustness to noisy input signals. Figure 4.3 shows the instantaneous phase and amplitude profile for one particular MZI signal realization, as estimated by the filter. Although both the amplitude and phase content can be used for calibration, the instantaneous phase was preferred in this work because it enables a simpler implementation of the asynchronous clock generation circuit.

4.1.2 CLK Generating Mechanism

The light intensity profile of the MZI output can be described by,

$$I_{MZI}(t) = CS(t)\cos(\phi(t)), \tag{4.8}$$

where C is a constant, S(t) is the spectral shape of the emitted laser beam and ϕ is the phase difference between the two photons added up on the receiver coupler in an MZI.

The extracted instantaneous phase, ϕ, is driving the comparator to generate a calibrating asynchronous clock (Fig. 4.4) [17]. The comparison step only fires up a positive edge when the phase is increased by a predefined value (Δ). This method will effectively generate positive edges of a clock signal whenever the phase is incremented by equal intervals.

[h] Extended Kalman Filter [11]

Initialization:

$\boldsymbol{P}_0 = \boldsymbol{I}\ (Identity\ matrix).\ \hat{\boldsymbol{x}}_0 = Initial\ estimate\ of\ the\ state\ space\ model.\ n = 1$

Time update:

$\hat{\boldsymbol{x}}_n^- = \boldsymbol{F}\hat{\boldsymbol{x}}_{n-1}\ \boldsymbol{P}_n^- = \boldsymbol{F}\boldsymbol{P}_{n-1}\boldsymbol{F}^T + \boldsymbol{V}$ *Measurement Update*:

$\boldsymbol{K}_n = \boldsymbol{P}_n^-\boldsymbol{H}_n^T\left(\boldsymbol{H}_n\boldsymbol{P}_n^-\boldsymbol{H}_n^T + \frac{\sigma_w^2}{2}\right)^{-1}.\ \hat{\boldsymbol{x}}_n = \hat{\boldsymbol{x}}_n^- + \boldsymbol{K}_n(y_n - \boldsymbol{H}_n).\ \boldsymbol{P}_n = (\boldsymbol{I} - \boldsymbol{K}_n\boldsymbol{H}_n)\boldsymbol{P}_n^-.$

close;

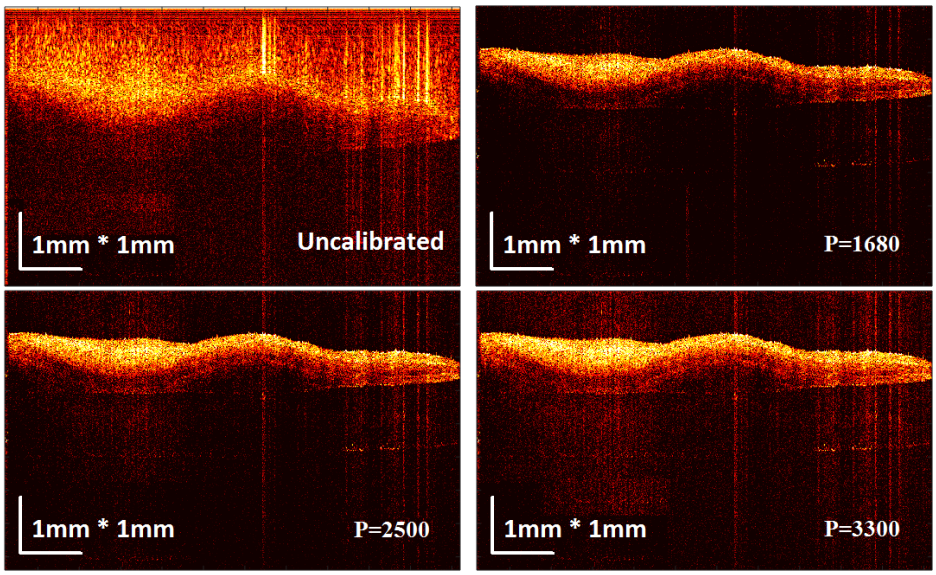

Figure 4.5: Image reconstruction comparison. (a) Uncalibrated. (b) through (d), increasing number of wavenumber quantization levels P.

4.2 Results

Performance of the presented algorithm was evaluated in terms of axial resolution, sensitivity roll-off and image reconstruction. Data for over 500 realizations was obtained for three different arm depths while modifying the P parameter (number of sampling points per MZI cycle); we also compared the performance of the algorithm against different ADC resolutions. Fig. 4.6 shows the mean axial resolution for 500 a-lines in terms of input ADC resolution and sample point number. Axial resolution remains constant throughout all tested ADC resolutions, implying that our proposed scheme can be used to significantly relax ADC specifications without resolution loss, which translates to an immediate power saving advantage. A single bit reduction can represent a power consumption reduction factor of at least four [14].

Finally we measured the sensitivity roll-off across seven sample arm depth indexes, as shown in Fig. 4.6. Sensitivity roll-off remained acceptably low throughout the entire

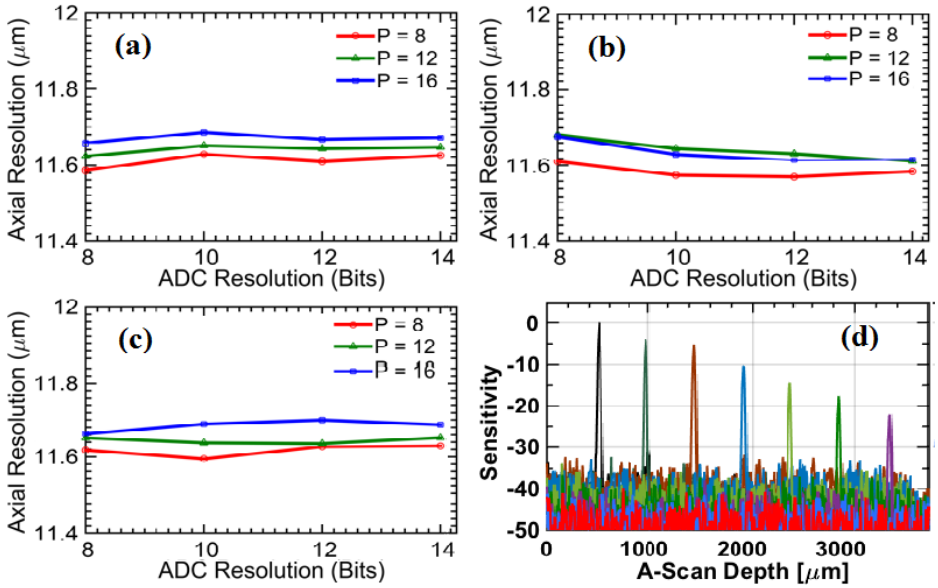

Figure 4.6: Axial Resolution mean value (a) to (c) Different sampling arm lengths (a:1448μm-b:1921μm-c:2361μm), across 500 realizations as a function of ADC Resolution (8bits-14bits) and P (d): sensitivity roll-off ($20log_{10}, dB$) across all depths.

imaging depth, without showing significant decay until after 1.5mm.

Our proposed resampling scheme exhibits results comparable to offline calibration methods while providing robustness to noise and efficiency, making it suitable for real-time, low cost SS-OCT implementations. While our in-house system was built for $30000, the state of the art commercial products can cost as high as $70000 (THORLABS, Part number : TEL1300V2).

In terms of image quality our results are on a par with those obtained by offline calibration methods. It can be clearly observed in Fig. 4.5 that for image reconstruction, the choice of P has little effect on the overall quality of the image.

4.3 Conclusion

We demonstrated a novel approach for the spectral calibration of low cost, noise prone, swept sources using a real-time estimation algorithm and a very simple sampling scheme

that allows for effortless determination of the number of sampling points needed in an B-scan. A corrected k-linearized clock is estimated from a simple Mach-Zehnder interferometer (MZI) and then used to non-uniformely sample the interferometer signal at the correct times. Axial resolution results were found to be on par with conventional spectral phase-based calibration techniques while significantly improving robustness, enabling future development of cost effective SS-OCT systems.

5. INTERPOLATED DISCRETE FOURIER TRANSFORM BASED CALIBRATION*

Instantaneous frequency and phase estimation of time varying signals has been investigated thoroughly in multidisciplinary applications including motor fault detection and RF demodulation. By pioneering in comparing various known IpDFT frequency estimation algorithms against the state of the art, this work aims to provide a comprehensive insight into on chip solution implementation for common SS-OCT processing techniques including calibration[31], dispersion correction, and background subtraction. Repeated application of IpDFT on buffered pieces of the Mach-Zehnder Interferometer (MZI) signal was first performed in this work to generate spectral frequency domain calibrating clock. As will be discussed further in the following sections, the significant inherent advantages of the proposed technique make it conclusively suitable for silicon based calibration solutions. Our simulations show a significant improvement in the execution time, dynamic and static memory for the recommended technique are both down due to less computation runtime and less complexity, respectively. The auxiliary circuitry needed to employ IpDFT is also much less convoluted than those of the Hilbert transformation as the phase extraction functions for the state of the art is reported to be extremely costly to be implemented. [21]

5.1 Setup

Data collection was implemented in a purposely built SS-OCT system comprised of a swept source with a center wavelength of 1310 nm at 150 kHz sweep rate (ESS, Exalos). Acquisition was performed using a 14-Bit 250 MS/s digitizer (NI5761, National Instruments).

*2017 IEEE. Reprinted, with permission, from O. Barajas, A. Tofighi Zavareh, and S. Hoyos, "High Performance Calibration Algorithm for Ultra High Speed Swept Source Optical Coherent Tomography", 2017 IEEE International Symposium on Circuits and Systems (ISCAS), 2017.

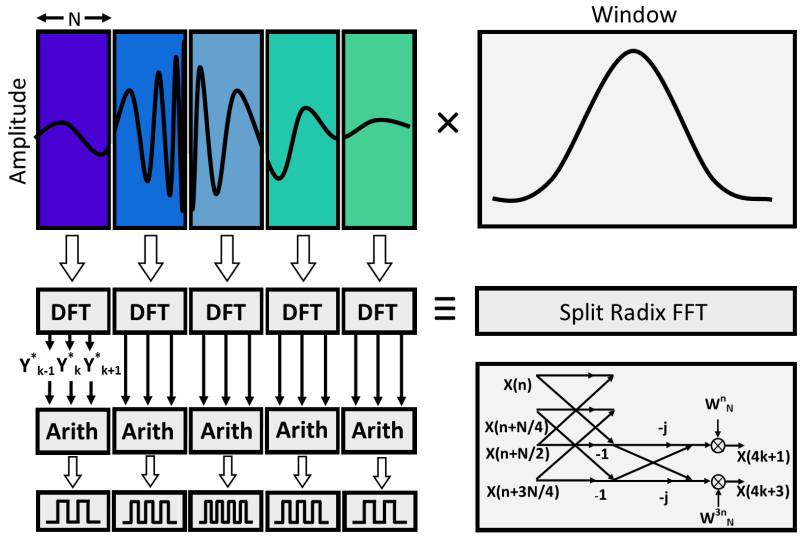

Figure 5.1: IpDFT algorithm implementation diagram, bottom right shows a split-radix FFT butterfly diagram.

5.2 IpDFT Implementation

Interpolated DFT (IpDFT) [21] is an established discrete Fourier transform based technique for the accurate calculation of the instantaneous parameters of a signal. IpDFT methods improve upon the fundamental problems exhibited by classical DFT algorithms such as spectral leakage, and can provide a faithful frequency estimation on small observation windows. In this work, the applicability of such algorithms for the calibration problem was thoroughly evaluated and implemented as follows: The MZI signal is acquired and buffered in blocks of size P, these get multiplied by an appropriate time window and lastly, an efficient split radix FFT [22] algorithm calculates the current block DFT bins so that a correct instantaneous frequency can be obtained via one of the proposed techniques in this section (Fig. 1).

Table 5.1: Computational complexity comparison of a Hilbert transformation based technique against IpDFT utilizing multiple windows and enhanced split radix FFT. Signal length is defined as N.

Techniques	*Hilbert*	*IpDFT [21]*	
	Order | L	Obs Window Length |	P
# Add / per output	L	P($\frac{4}{3}log_2$(P)-$\frac{8}{9}$)-$\frac{1}{9}$(-1)$^{log_2(P)}$	
# Mult / per output	L	P($\frac{2}{3}log_2$(P)-$\frac{19}{9}$)+$\frac{1}{9}$(-1)$^{log_2(P)}$	
# Total Arithmetic	2LN	$\frac{N}{P}$(2Plog_2P-3P)	

5.2.1 Time Windows

Time window properties can be evaluated by their main lobe width and side lobe attenuation. While the former is designed to be narrower to increase the estimation resolution, the latter tends to be as big as possible to minimize the spectral leakage.

These trade-offs should be taken into account when the length of a window is chosen. Higher order Rife-Vincent Class I (RVCI) windows may result in negligible estimation error because of the fast side lobe decay. Still, the signal needs to contain enough number of periods due to wide main lobe of such windows. Although the systematic errors for Kaiser-Bessel and Dolph-Chebyshev windows are significantly higher than high order RVCI windows due to lower side lobe decay rate, they can provide a better frequency estimation for signals with 2-4 cycles. It should be noted that the use of time windows can be eliminated in some IpDFT techniques such as Bertocco-Yoshida.

5.2.1.1 Background Theory

The MZI signal at any buffered block is modeled by,

$$y[n] = Acos(\omega_0 n + \phi)e^{-dn} = \frac{A}{2}\left(e^{-dn}e^{j(\omega_0 n+\phi)} + e^{-dn}e^{-j(\omega_0 n+\phi)}\right), \tag{5.1}$$

Table 5.2: Multiplication algorithms complexity, log^* stands for iterated logarithm.

Techniques	*Multiplication*	
	Order	N
Furer's algorithm [23]	**O**$(Nlog(N)\ 2^{\mathbf{O}(log^*(N))})$	
Schonhage Strassen algorithm [24]	**O**$(Nlog(N)log(log(N)))$	
Mixed level Toom-Cook [25]	**O**(N $2^{\sqrt{2log(N)}}log(N)$)	

Table 5.3: Comparison between the complexity of auxiliary blocks needed for Hilbert transformation techniques and IpDFT. M(N) below stands in for the complexity of the chosen multiplication algorithm.

Hilbert		*IpDFT*	
Tangent Inverse		Max Bin Det	
Taylor series; FFT-based acceleration [26]	**O**$(M(N)N^{1/3}\ log^2(N))$	Compare in Pairs	**O**(P)
Arithmetic-geometric mean iteration [27]	**O**$(M(N)log(N))$	Tournament Method	**O**(P)
Taylor series; binary splitting + bit burst [28]	**O**$(M(N)log^2(N))$	Linear search	**O**(P)

where d is the damping factor and ω_0 is the center frequency. It can be shown that the DFT of the first term in the right hand side of Eqn. (5.1) can be written as,

$$DFT\{e^{-dn}e^{j(\omega_0 n+\phi)}\} = e^{j\phi}\frac{1-e^{(j\omega_0-j\omega_k-d)P}}{1-e^{j\omega_0-j\omega_k-d}}, \tag{5.2}$$

and the entire DFT can be approximated as,

$$Y_k \approx \frac{A}{2}\left(e^{j\phi}\frac{1-\lambda^P}{1-\lambda e^{-j\omega_k}}\right), \quad 0 \leq \omega < \pi, \tag{5.3}$$

where $\lambda = e^{-d+j\omega_0}$. Y_k^* is the maximum height bin in the corresponding DFT vector. k denotes the bin index at which the maximum bin lands.

5.2.1.2 Betrocco-Yoshida (BY-2) algorithm

Let us assume that the adjacent bins to Y_k^* are ordered as Y_{k-1}^* being the highest followed by , Y_{k+1}^*, and Y_{k-2}^*. The value of λ can be proven to be,

$$\lambda = e^{j\omega_k} \frac{1-R}{e^{-j2\pi/P} - Re^{-j2(2\pi/P)}}, \tag{5.4}$$

where,

$$R = \frac{Y_{k-2}^* - 2Y_{k-1}^* + Y_k^*}{Y_{k-1}^* - 2Y_k^* + Y_{k+1}^*}. \tag{5.5}$$

In the case where the highest adjacent bin is Y_{k+1}^* followed by Y_{k-1}^* and Y_{k+2}^*,

$$\lambda = e^{j\omega_k} \frac{1-R}{e^{-j2(2\pi/P)} - Re^{-j2\pi/P}}, \tag{5.6}$$

where,

$$R = \frac{Y_{k-1}^* - 2Y_k^* + Y_{k+1}^*}{Y_k^* - 2Y_{k+1}^* + Y_{k+2}^*}. \tag{5.7}$$

Following the discussion above, ω_0 = Im{Ln(λ)}, and d = Re{Ln(λ)}.

5.2.1.3 RVCI windows (Order M)

IpDFT algorithms can be analytically derived for RVCI windows. In these algorithms a RVCI window is multiplied to each chunk of the data the instantaneous parameters are calculated for,

$$y[n] = w_n x_n = w_n A cos(\omega_0 n + \phi) e^{-dn} = \bar{w}_n A cos(\omega_0 n + \phi). \tag{5.8}$$

After taking the DFT from the buffered signals, the parameters R_1 and R_2 are defined as,

$$\begin{aligned} R_1 &= \frac{\|Y^*_{k+1}\|^2}{\|Y^*_k\|^2} \approx \frac{(\delta+M)^2+D^2}{(\delta-M-1)^2+D^2}, \\ R_2 &= \frac{\|Y^*_{k-1}\|^2}{\|Y^*_k\|^2} \approx \frac{(\delta-M)^2+D^2}{(\delta+M+1)^2+D^2}, \end{aligned} \tag{5.9}$$

where $D = dP/(2\pi)$. Computing the mentioned ratios, δ can be calculated as,

$$\delta = -\frac{2M+1}{2}\frac{R_1-R_2}{2(M+1)R_1R_2-R_1-R2-2M}. \tag{5.10}$$

From (5.9) the damping factor is,

$$\begin{aligned} d &= \frac{2\pi}{P}\sqrt{\frac{(\delta+M)^2-R_1(\delta-M-1)^2}{R_1-1}}, \qquad \delta > 0, \\ d &= \frac{2\pi}{P}\sqrt{\frac{(\delta-M)^2-R_2(\delta+M+1)^2}{R_2-1}}, \qquad \delta < 0. \end{aligned} \tag{5.11}$$

The parameter ω_0 then is going to be equal to $(k+\delta)\frac{2\pi}{P}$.

It should be noted that RVCI window order zero is called a rectangular window and the same kind with an order two is called Hanning window. [21]

5.2.1.4 Clock generation

Knowing the instantaneous frequency of each block of size P, a sampling clock was generated by creating a piecewise linear signal with the slope of each line being proportional to the next transitory frequency of the MZI. Previously proposed continuous-time level sampling techniques in [29] are used to collect the correct sampling time stamps.

5.2.2 Algorithmic Complexity Comparison

This section compares the complexity of state of the art Hilbert transformation techniques with IpDFT based techniques in terms of core arithmetic complexity and auxiliary operations needed for calibration.

5.2.2.1 Core Operation Time/Arithmetic Complexity

Until now, the most efficient reported techniques for the spectral calibration of SS-OCT systems involved the use of FIR Hilbert transformers as a core block. For the IpDFT algorithms, the main block consists of a split radix DFT block with a signal length of P performed on blocks of the MZI signal.

As Table 5.1 shows, an FIR filter with an order L needs L additions and L multiplications for each output sample to be executed. For a MZI signal of length N that implies a total arithmetic operations count of 2LN. To perform the DFTs in IpDFT, we used an efficient split-radix algorithm. The complexity and the number of additions and multiplications needed to perform the algorithm is shown in Table 5.1.

In the case of our application the signal length N was 3584 and the observation window length P, was chosen to be 64 samples. The state of the art Hilbert transformation technique in literature [30] uses 17 FIR filter coefficients to implement Hilbert transformation. Simple arithmetic calculations yield that Hilbert transformation based technique needs 121856 operations to compute the analytic signal while the proposed method only uses 32256 operations. It should be stated that a split radix needs only $log_2(P)$ clock cycles to be computed for each instantaneous phase sample, while Hilbert transform takes L clock cycles.

5.2.2.2 *Auxiliary Operations Time/Arithmetic Complexity*

In order to obtain the instantaneous phase using Hilbert transformation, an additional inverse tangent step needs to be performed on the analytical signal. It is worth noting that inverse tangent is a particularly difficult and inefficient operation to implement. Determination of inverse tangent algorithm complexity can itself be intricate, as the overall number of operations is a function of the chosen multiplication type; to give the reader a sense of the overall inverse tangent complexity, some notable multiplication algorithms are included in Table. 5.2, while Table. 5.3 contains applicable algorithms for inverse tangent determination. For IpDFT however, the only extra auxiliary operation needed is maximum DFT bin determination. Table 5.3 clearly shows that performing inverse tangent is significantly more complex than the techniques used to find the maximum DFT bin.

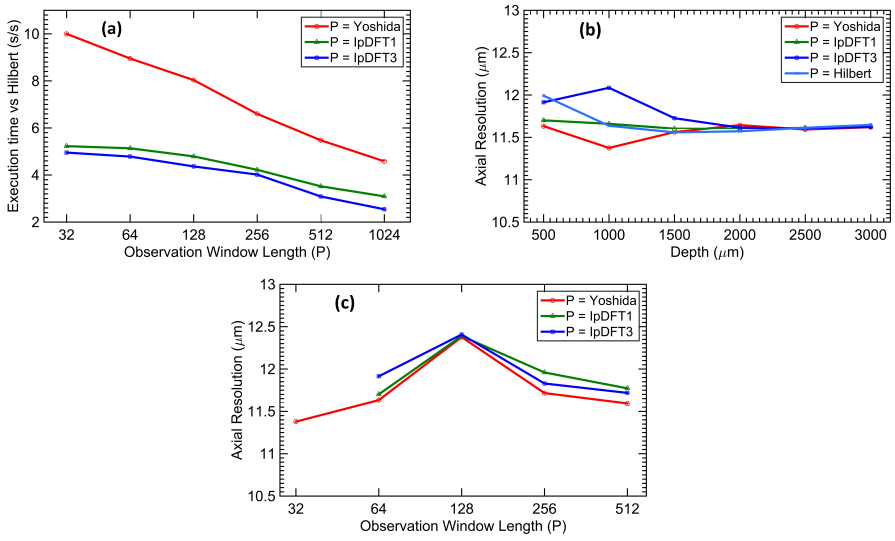

Figure 5.2: (a) Normalized execution time compared to Hilbert transformation vs. Observation window length, (b) Axial resolution compared to sample arm depth, (c) Axial resolution vs. Observation window length.

5.3 Results

The proposed algorithm performance was evaluated in terms of axial resolution, execution time, and image quality. Figure 5.2(a) shows the normalized execution time for 500 interferometer realizations compared to Hilbert transformation. It can be easily observed that Betrocco-Yoshida (BY-2) algorithm is by far the most efficient, outperforming Hilbert for up to a factor of ten depending of chosen P factor. The logarithmic behaviour predicted in Table 5.1 can also be observed from Figure 5.2.

To evaluate the axial resolution, 500 A-scans were acquired from a mirror sample at 5 different arm depths for all three different IpDFT methods. As shown in Figure 5.2(b), the Yoshida algorithm also exhibits the best result in terms of axial resolution up to an observation window length of 64.

As shown in Figure 5.2(c), observation window length was swept across all proposed calibration methods in order to determine its optimum size; generally, an ascending trend in axial resolution was observed as window length increased. It can also be observed that for IpDFT1 and IpDFT3, at least 64 samples are needed for calibration to be performed. The designer needs to always keep in mind that extremely short windows can not spot the temporal specifications of the MZI.

Figure 5.3 shows the cross sectional image of a biological tissue calibrated by different techniques. Buffer size was chosen to be 64 in order to accurately compare all methods.

5.4 Conclusion

We demonstrated the superiority of Interpolated Discrete Fourier Transform (IpDFT) based algorithms over state of the art FIR Hilbert calibration techniques for the spectral calibration of SS-OCT systems. Bertocco-Yoshida (BY-2) decisively exhibited improved results in terms of efficiency, complexity and axial resolution. More importantly, we laid foundational work for future low cost, system on chip solutions for SS-OCT calibration

and other necessary signal conditioning steps, eventually leading to substantial cost and power advantages.

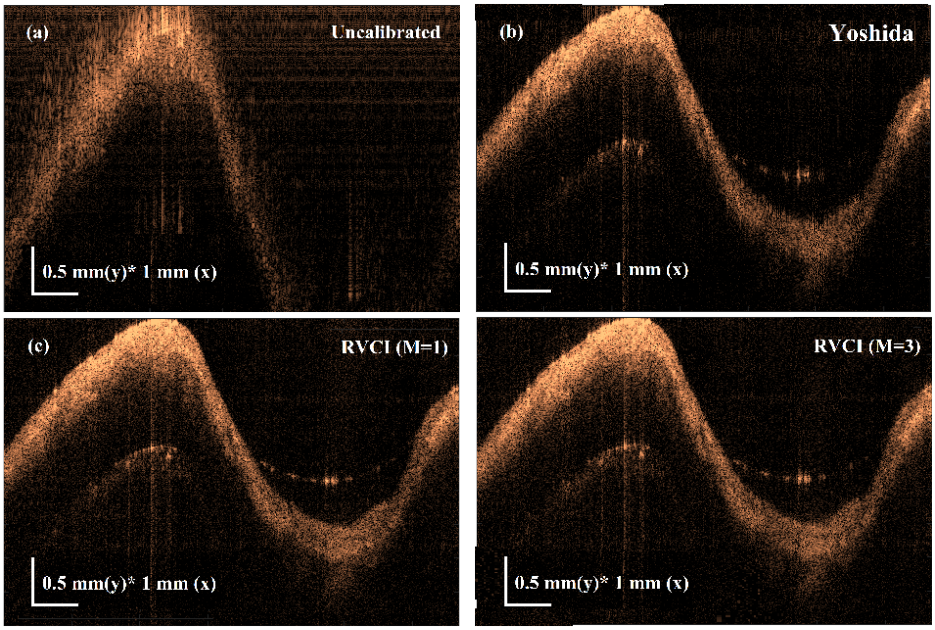

Figure 5.3: Image reconstruction comparison. (a) Uncalibrated. (b) Bertocco-Yoshida (BY-2) (c) RVCI (M=1) (d) RVCI (M=3)

6. SUMMARY AND CONCLUSIONS

Swept Source Optical Coherence Tomography has recently become the de-facto imaging technique when high axial resolution is needed in low penetration applications. With the recent advancements on swept source technology and volumetric microscopy imaging, new challenges in terms of processing and storage of large datasets have emerged. In this thesis, a multitude of spectral calibration algorithms were presented, all attempting to face one of the main identified challenges surrounding SS-OCT technology: Ultra-Fast processing for MHz SS-OCT, Low data throughput for fast and efficient C-Scan generation and noise tolerance for novel cost effective swept source implementations like MEMS-less VCELS. Promising results were exhibited by all the techniques in their respective application.

6.1 Challenges

A comprehensive study needs to be performed to identify the key challenges and opportunities regarding the development of efficient signal processing of solutions for SS-OCT systems, preliminary research indicates such algorithms may contribute to the development of low cost, all inclusive solutions for the spectral calibration of SS-OCT systems.

6.2 Further Study

A hardware implementation is currently being validated on an FPGA platfrom to investigate the real world application of the techniques developed in this work.

BIBLIOGRAPHY

[1] E. Azimi, B. Liu, and M. E. Brezinski, "Real-time and high-performance calibration method for high-speed swept-source optical coherence tomography," Journal of Biomedical Optics, vol. 15, no. 1, p. 016005, 2010.

[2] C. N. Copeland and A. K. Ellerbee, "Analysis of the effects of different resampling techniques for optical coherence tomography," Three-Dimensional and Multidimensional Microscopy: Image Acquisition and Processing XIX, vol. 8227, 2012.

[3] R. K. Meleppat, M. V. Matham, and L. K. Seah, "An efficient phase analysis-based wavenumber linearization scheme for swept source optical coherence tomography systems," Laser Physics Letters, vol. 12, no. 5, p. 055601, Apr. 2015.

[4] R. K. Manapuram, V. G. R. Manne, and K. V. Larin, "Phase-sensitive swept source optical coherence tomography for imaging and quantifying of microbubbles in clear and scattering media," Journal of Applied Physics, vol. 105, no. 10, p. 102040, 2009.

[5] T. Wu, Z. Ding, L. Wang, and M. Chen, "Spectral phase based k-domain interpolation for uniform sampling in swept-source optical coherence tomography," Optics Express, vol. 19, no. 19, p. 18430, Sep. 2011.

[6] J. Xi, L. Huo, J. Li, and X. Li, "Generic real-time uniform k-space sampling method for high-speed swept-source optical coherence tomography," Optics Express, vol. 18, no. 9, p. 9511, Apr. 2010.

[7] J. Zhou, M. Ramirez, S. Palermo, and S. Hoyos, "Digital-assisted Asynchronous compressive sensing front-end," IEEE Journal on Emerging and Selected Topics in Circuits and Systems, vol. 2, no. 3, pp. 482âĂŞ492, Sep. 2012.

[8] K. P. Zetie, S. F. Adams, and R. M. Tocknell, "How does a Mach-Zehnder interferometer work?," Physics Education, vol. 35, no. 1, pp. 46âĂŞ48, Jan. 2000.

[9] R. H. Walden, "Analog-to-digital converter survey and analysis," IEEE Journal on Selected Areas in Communications, vol. 17, no. 4, pp. 539âĂŞ550, Apr. 1999.

[10] S. Kim, P. D. Raphael, J. S. Oghalai, and B. E. Applegate, "High-speed spectral calibration by complex FIR filter in phase-sensitive optical coherence tomography," Biomedical Optics Express, vol. 7, no. 4, p. 1430, Mar. 2016.

[11] D. Huang et al., Optical coherence tomography, Science, vol. 254, no. 5035, pp. 1178-1181, 1991.

[12] C. D. Lu et al., Handheld ultrahigh speed swept source optical coherence tomography instrument using a MEMS scanning mirror, Biomedical Optics Express Biomed. Opt. Express, vol. 5, no. 1, p. 293, 2013.

[13] L. S. Lim et al., Comparison of spectral domain and swept-source optical coherence tomography in pathological myopia, Eye, vol. 28, no. 4, pp. 488âĂŞ491, 2014.

[14] 2016 IEEE. Reprinted, with permission, from A. T. Zavareh, O. Barajas, M. Serafino, J. Jo, B. Applegate, B. M. Sadler, and S. Hoyos, "A novel continuous time ternary encoding based SS-OCT calibration," 2016 IEEE Biomedical Circuits and Systems Conference (BioCAS), 2016.

[15] J. Gal, et al., The estimation of chirp signals parameters by an extended Kalman filtering algorithm ISSCS 2011 - International Symposium on Signals, Circuits and Systems, 2011.

[16] G. F. Lawler and V. Limic, Random walk: a modern introduction. Cambridge: Cambridge University Press, 2010.

[17] Mark, J., and T. Todd. "A Nonuniform Sampling Approach to Data Compression." IEEE Transactions on Communications 29.1 (1981): 24-32.

[18] A. Petzold, Optical coherence tomography in multiple sclerosis: clinical applications. Cham: Springer, 2016.

[19] J. A. Izatt and M. A. Choma, "Theory of Optical Coherence Tomography," Optical Coherence Tomography Biological and Medical Physics, Biomedical Engineering, pp. 47–72.

[20] A. T. Zavareh et al., "A novel continuous time ternary encoding based SS-OCT calibration," 2016 IEEE Biomedical Circuits and Systems Conference (BioCAS), Shanghai, 2016, pp. 5-8. doi: 10.1109/BioCAS.2016.7833711

[21] K. Duda, "Interpolation Algorithms of DFT for Parameters Estimation of Sinusoidal and Damped Sinusoidal Signals," Fourier Transform - Signal Processing, Nov. 2012.

[22] S. G. Johnson and M. Frigo, "A modified Split-Radix FFT with fewer arithmetic operations," IEEE Transactions on Signal Processing, vol. 55, no. 1, pp. 111–119, Jan. 2007.

[23] M. FuÃijrer, "Faster Integer Multiplication," SIAM Journal on Computing, vol. 39, no. 3, pp. 979–1005, 2009.

[24] A. Schonhage and V. Strassen, "Schnelle Multiplikation groÃ§er Zahlen," Computing, vol. 7, no. 3-4, pp. 281–292, 1971.

[25] M. T. Mcclellan, J. Minker, and D. E. Knuth, "The Art of Computer Programming, Vol. 2: Seminumerical Algorithms," Mathematics of Computation, vol. 2, 1974.

[26] B. C. Berndt, J. M. Borwein, and P. B. Borwein, "Pi and the AGM–A Study of Analytic Number Theory and Computational Complexity.," Mathematics of Computation, vol. 50, no. 181, p. 352, 1988.

[27] R. P. Brent, "Multiple-Precision Zero-Finding Methods And The Complexity Of Elementary Function Evaluation," Analytic Computational Complexity, pp. 151–176, 1976.

[28] D. V. Chudnovsky and G. V. Chudnovsky, "and complex multiplication according to Ramanujan," Pi: A Source Book, pp. 596–622, 1988.

[29] 2017 IEEE. Reprinted, with permission, from A. T. Zavareh, O. Barajas and S. Hoyos, "An Efficient Estimitaion Algorithm for the Calibration of Low-Cost SS-OCT Systems," 2017 IEEE 14th International Symposium on Biomedical Imaging (ISBI), Melbourne, Australia, 2017.

[30] S. Kim, P. D. Raphael, J. S. Oghalai, and B. E. Applegate, "High-speed spectral calibration by complex FIR filter in phase-sensitive optical coherence tomography," Biomedical Optics Express, vol. 7, no. 4, p.1430, Mar. 2016.

[31] 2017 IEEE. Reprinted, with permission, from O. Barajas, A. Tofighi Zavareh, and S. Hoyos, "High Performance Calibration Algorithm for Ultra High Speed Swept Source Optical Coherent Tomography", 2017 IEEE International Symposium on Circuits and Systems (ISCAS), 2017.

[32] J. Zhou; A. Tofighi Zavareh; R. Gupta; L. Liu; Z. Wang; B. M. Sadler; J. Silva-Martinez; S. Hoyos, "Compressed Level Crossing Sampling for Ultra-Low Power IoT Devices," in IEEE Transactions on Circuits and Systems I: Regular Papers , vol.PP, no.99, pp.1-13 doi: 10.1109/TCSI.2017.2707481

[33] Meena Siddiqui and Benjamin J. Vakoc, "Optical-domain subsampling for data efficient depth ranging in Fourier-domain optical coherence tomography," 2012, Opt. Express 20, 17938-17951

[34] A. Podoleanu, "Optical coherence tomography", Journal of Microscopy, vol. 247, no. 3, pp. 209-219, 2012.

[35] S. Yun, G. Tearney, B. Vakoc, M. Shishkov, W. Oh, A. Desjardins, M. Suter, R. Chan, J. Evans, I. Jang, N. Nishioka, J. de Boer and B. Bouma, "Comprehensive volumetric optical microscopy in vivo", 2017.